

JGR Space Physics

RESEARCH ARTICLE

10.1029/2020JA028173

Special Section:

Early Results From the Global-Scale Observations of the Limb and Disk (GOLD) Mission

Key Points:

- Derivation of zonal drift velocities of EPBs observed by GOLD from geostationary orbit
- First simultaneous measurement of EPBs zonal drift velocities at the equator and both crests of the equatorial ionization anomaly (EIA)
- Zonal drift velocities of EPBs at the equator and EIA crests are equal

Supporting Information:

- · Supporting information S1
- · Figure S1
- · Figure S2

Correspondence to:

D. K. Karan, deepak.karan@lasp.colorado.edu

Citation:

Karan, D. K., Daniell, R. E., England, S. L., Martinis, C. R., Eastes, R. W., Burns, A. G., & McClintock, W. E. (2020). First zonal drift velocity measurement of equatorial plasma bubbles (EPBs) from a geostationary orbit using GOLD data. *Journal of Geophysical Research: Space Physics, 125*, e2020IA028173. https:// doi.org/10.1029/2020JA028173

Received 28 APR 2020 Accepted 13 AUG 2020 Accepted article online 21 AUG 2020

First Zonal Drift Velocity Measurement of Equatorial Plasma Bubbles (EPBs) From a Geostationary Orbit Using GOLD Data

Deepak K. Karan¹ D, Robert E. Daniell², Scott L. England³ D, Carlos R. Martinis⁴ D, Richard W. Eastes¹ D, Alan G. Burns⁵ D, and William E. McClintock¹ D

¹Laboratory for Atmospheric and Space Physics, University of Colorado, Boulder, CO, USA, ²Ionospheric Physics, Stoughton, MA, USA, ³Virginia Polytechnic Institute and State University, Blacksburg, VA, USA, ⁴Center for Space Physics, Boston University, Boston, MA, USA, ⁵High Altitude Observatory, Boulder, CO, USA

Abstract The National Aeronautics and Space Administration (NASA) Global-scale Observations of the Limb and Disk (GOLD) satellite takes far-ultraviolet images of the Earth from geostationary orbit. GOLD observes the complete structure of equatorial plasma bubbles (EPBs). Since there are repeated observations of the same regions of the Earth, the zonal drift velocities of EPBs are derived using GOLD data. EPBs observed within 60– 25° W longitudes on 27–29 November 2018 are considered in the present analysis. The drift velocities obtained on 27 November 2018 are 116 ± 4 , 118 ± 6 , and 105 ± 9 m/s at the North and South crests of equatorial ionization anomaly (EIA) and the magnetic equator, respectively. While on 29 November the velocities 107 ± 10 , 106 ± 8 , and 110 ± 4 m/s are in agreement with the 27th (within the uncertainties), on 28 November the velocities are substantially lower: 80 ± 3 , 95 ± 7 , and 88 ± 11 m/s. This is the first simultaneous measurement of EPB zonal drift velocities at both crests of EIA and the magnetic equator. On 27–29 November 2018, the average spacing between adjacent EPBs is found to be ~377, 526, and

Plain Language Summary After the sunset, the ionosphere becomes conducive to the formation of plasma irregularities. These irregularities are associated with depletions in the plasma density. In the images obtained from ground or space, these depleted regions look like elongated dark bands and are known as "equatorial plasma bubbles (EPBs)." The transionospheric radio wave propagation, satellite communication, and navigation systems are adversely affected by these bubbles. Thus, it is important to understand and investigate the formation and development of the plasma bubbles. These have been extensively studied using ground-based instruments and satellites. However, all of these techniques are limited to short time observations and small spatial coverage. NASA's Global-scale Observations of the Limb and Disk (GOLD) satellite has brought the unique opportunity to observe the Earth's complete disk continuously from the geostationary orbit. In the present study, zonal drift velocities of EPBs are derived from the data obtained by GOLD from geostationary orbit. Further, for the first time, EPB drift velocities are derived simultaneously at crests of the EIA and at the geomagnetic equator.

1. Introduction

Equatorial plasma bubbles (EPBs), a nighttime plasma irregularity phenomenon, occur within the equatorial and low-latitude ionosphere due to the horizontal orientation of the magnetic field lines in this region (Fejer & Kelley, 1980). Transionospheric radio wave propagation for communication and navigation is adversely affected when passing through the plasma irregularities in the region. This makes the investigation of ionospheric irregularities an important, societally relevant priority for researchers. After sunset, the bottom side of the ionosphere recombines faster, due to higher ion-neutral collision frequencies than the topside. Also, due to prereversal enhancement (PRE) of the zonal electric field, the ionosphere moves upward during this time period; these effects produce a sharp gradient in electron density. This configuration is similar to the situation where a heavier fluid layer is supported by a lighter one. Such a situation is dynamically unstable and can lead to the well-known Rayleigh-Taylor Instability (RTI). Any perturbations in the depleted (enhanced) density at the bottom side of the ionosphere will move upward (downward) (Kelley, 2009). While moving upward, the depleted plasma density regions

©2020. American Geophysical Union. All Rights Reserved.

KARAN ET AL. 1 of 11



(depletions) modify the vertical electron density distributions and cause plasma irregularities in the region of their occurrence. The cause for the perturbations at the bottom layer is still a topic of debate, and such perturbations are thought to "seed" the plasma irregularities. Sometimes the daytime ionospheric and thermospheric coupling processes and wave activity make the ionosphere conducive to the occurrence of nighttime plasma irregularities (Karan et al., 2016; Karan & Pallamraju, 2020; Mandal et al., 2019; Pallamraju et al., 2004, 2016; Sridharan et al., 1994). The depleted plasma density regions (depletions) can grow nonlinearly and rise to 500-1,500 km (Anderson & Mendillo, 1983). At the same time, the depleted plasma region expands along the magnetic field lines on each side of the geomagnetic equator. Typically, the depletions also drift eastward due to vertical polarization electric fields associated with the zonal neutral winds in the F region (Anderson & Mendillo, 1983; Kelley, 2009; Makela, 2006; Martinis et al., 2003).

Nighttime plasma irregularities over equatorial and low latitudes have been studied using different observational techniques from the ground and space. Different terminologies have been used to describe the observed effects. For digisonde observations, "spread-F" is used; "scintillations" and "plumes" are used for radar measurements; in satellite literature, "bite outs," "depletions," and "bubbles" are common terms; in optical imaging "bubbles"; and in models, "depleted magnetic flux tubes" and "bubbles" are often used. In the present study, the term EPBs is used.

Different approaches have been used to investigate various aspects of EPBs. Latitudinal and seasonal variations of the zonal drifts have been studied with ground-based radar measurements (Abdu et al., 1981, 1985; Basu et al., 1996; Kil et al., 2002; Valladares et al., 2002). Investigations have been carried out to study the occurrence rates of plasma depletions for different seasons and local times using GUVI (Global Ultraviolet Imager) data (Henderson et al., 2005; Sahai et al., 1994). Observations from DMSP (Defense Meteorological Satellite Program), ROCSAT-1 (Republic of China Satellite), C/NOFS (Communications/ Navigation Outage Forecasting System), and COSMIC (Constellation Observing System for Meteorology, Ionosphere, and Climate) have been used to study the longitudinal variability (Burke et al., 2004), formation and evolution (Huang et al., 2011), and global climatology of EPBs (Kepkar et al., 2019). Conjugacy of EPBs (Shiokawa et al., 2004, 2015), a reversal in the drift directions (Taylor et al., 1997), and bifurcation and merging of EPBs (Mendillo & Tyler, 1983) are observed in ground-based imaging techniques. Such features of EPBs are also studied through theoretical modeling (Huba et al., 2015; Huba & Liu, 2020; Huba & Joyce, 2007; Zalesak et al., 1982). Further, numerical computational modeling (Zalesak et al., 1982; Sekar, 2003, and references therein) and empirical modeling (England & Immel, 2012) have been carried out to understand the formation, growth, and characteristics of EPBs. Growth rates of EPBs have been studied through data assimilation and modeling (Rajesh et al., 2017). Aa et al. (2020) have reported coordinated ground and space-based observation of EPBs.

Measurements of zonal drift velocities of EPBs are of interest to researchers since they give ionospheric electric field information. Ground-based, scanning photometers (Sobral & Abdu, 1991) and optical, all-sky imagers at different emission wavelengths, for example, OI 557.7, 630.0, and 777.4 nm (Chapagain et al., 2012; Gurav et al., 2019; Hickey et al., 2018; Martinis et al., 2003; Mendillo et al., 1997; Mendillo & Baumgardner, 1982; Narayanan et al., 2017; Pimenta et al., 2001; Sinha & Raizada, 2000; Taylor et al., 1997) have been extensively used to study the zonal drift velocities of EPBs. In such measurements, zonal motion of the airglow depletions is considered to be equal to the ambient plasma drift. However, this need not be the case in the early phase of the irregularities, since during this time the growth is highly nonlinear in the bottom side ionosphere (Martinis et al., 2003). Immel et al. (2003) presented a method to determine the drift velocity of the plasma bubbles using the Imager for Magnetopause-to-Aurora Global Exploration-far ultraviolet (IMAGE-FUV) Imager data. They used keogram analysis to derive the drift velocities. This was extended by Park et al. (2007) to automate and permit detection of variations with latitude. England and Immel (2012) used this method to produce an empirical model of the drift velocities, showing variations with latitude and local time. A real challenge faced with IMAGE was that as a result of orbital precession the low latitudes in the early evening were only visible for a few months in 2002 and 2003. During these months, the viewing geometry was such that only the northern airglow arc could typically be seen. While IMAGE could observe the same EPB more than once, GUVI on the TIMED (Thermosphere Ionosphere Mesosphere Energetics and Dynamics) satellite could observe an EPB only once which is insufficient for obtaining the drift velocities of EPBs (Park et al., 2007).

KARAN ET AL. 2 of 11



Ground-based optical observations have limited spatial coverage and are limited to clear sky conditions. While low Earth-orbiting satellites can provide observations every orbit (~90 min), they have limited spatial coverage and are constrained by the viewing angle. Due to these difficulties, simultaneous measurements of drift velocities of EPBs at both crests of EIA and the magnetic equator have not been possible until now, to the best of our knowledge.

NASA's Global-scale Observations of the Limb and Disk (GOLD) mission observes Earth's FUV airglow emissions from geostationary orbit (Cai et al., 2020; Eastes et al., 2017, 2019, 2020). Disk observations by the GOLD spectrograph provide unique opportunity for more detailed information about EPBs. In the present study, we have derived the zonal drift velocity of EPBs over the South American longitude region using GOLD data. The zonal drift velocities of EPBs are obtained simultaneously at both crests of the EIA and the magnetic equator.

2. GOLD Observations and Data

The GOLD satellite was launched on 25 January 2018 and is located in geostationary orbit at 47.5°W (near the mouth of the Amazon river). Nominal operations and observations started on 9 October 2018. The main goals of GOLD are (i) to study how Earth's ionosphere-thermosphere system responds to the geomagnetic storm, solar forcing, and lower atmospheric waves and (ii) investigation of formation and evolution of ionospheric plasma irregularities (Eastes et al., 2017, 2019). GOLD has two identical spectrographs that obtain images of the Earth at FUV (~132-162 nm) emission wavelength. GOLD measures the column integrated emission rate along the line of sight. GOLD has the advantage of observing the American, Atlantic, and Western African longitudinal regions. This provides a unique opportunity to unambiguously observe the spatial temporal evolution of various ionospheric-thermospheric features of the Earth visible to GOLD. GOLD takes entire disk observation, limb scans, and occultations. L1C is the science data product of GOLD, which is used in this work. The L1C daytime disk images of the Earth are obtained with a cadence of 30 min and binned to a spatial resolution of 125 km × 125 km at nadir. The night time L1C disk images are obtained at a cadence of 15 min and binned to a spatial resolution of 96 km × 80 km at nadir. Limb images are obtained above the equatorial limbs up to ~430 km height with an altitude grid of ~20 km. Stellar occultation measurements are taken at an altitude of ~225 km above the surface of Earth at the latitude of occultation (McClintock et al., 2020). Detail information about the GOLD instrument, observation mode, and data products with some initial observations are discussed in Eastes et al. (2017, 2020) and McClintock et al. (2020). Only the nighttime disk images of OI 135.6 nm (NI1 data) are used in the present study. The night time peak emission altitude for OI 135.6 nm is considered to be 300 km when geolocating the pixels.

3. Results

GOLD takes nighttime disk observations using both channels A and B (CHA and CHB hereafter). An image is obtained in every 15 min, initially over the African sector, and follows the sunset terminator towards the American sector. The number of steps (slit positions) and dwell time varies from image to image. As a result, the longitudinal coverage in each image is different (it varies from 23° to 40° at the geographic equator). Starting from 20:10 UT, CHB takes the night disk images alternating between Northern and Southern Hemispheres. However, simultaneous observations from the Northern and Southern hemispheres are made from 23:10 to 00:09 UT, using CHA and CHB. After 1 January 2019, such simultaneous observations are made till 00:25 UT. Both images are obtained at nearly the same longitude region. Hence, during this 1 hr of observations on each day, it is possible to observe EPBs completely as these are extended to both hemispheres across the geomagnetic equator. The sequence of nighttime scans as described above is replicated on each night. Such unique observations provide an opportunity to study the complete morphology and motion of EPBs. In the present study, observations obtained during this 1 hr period on 27–29 November 2018 are used.

Simultaneous images obtained by CHA and CHB from Northern and Southern Hemispheres during 23:10-00:09 UT on 28 November 2018 (DOY = 332) are shown in Figure 1. The horizontal and vertical axes show geographic longitudes and latitudes. Figures 1a-1d show the images obtained at 23:10, 23:25, 23:40, and 23:55 UT, respectively. The bright emissions along the equatorial ionization anomaly (EIA) crests can clearly be seen. Notice the decrease in brightness along the multiple EPBs at each image. GOLD takes

KARAN ET AL. 3 of 11

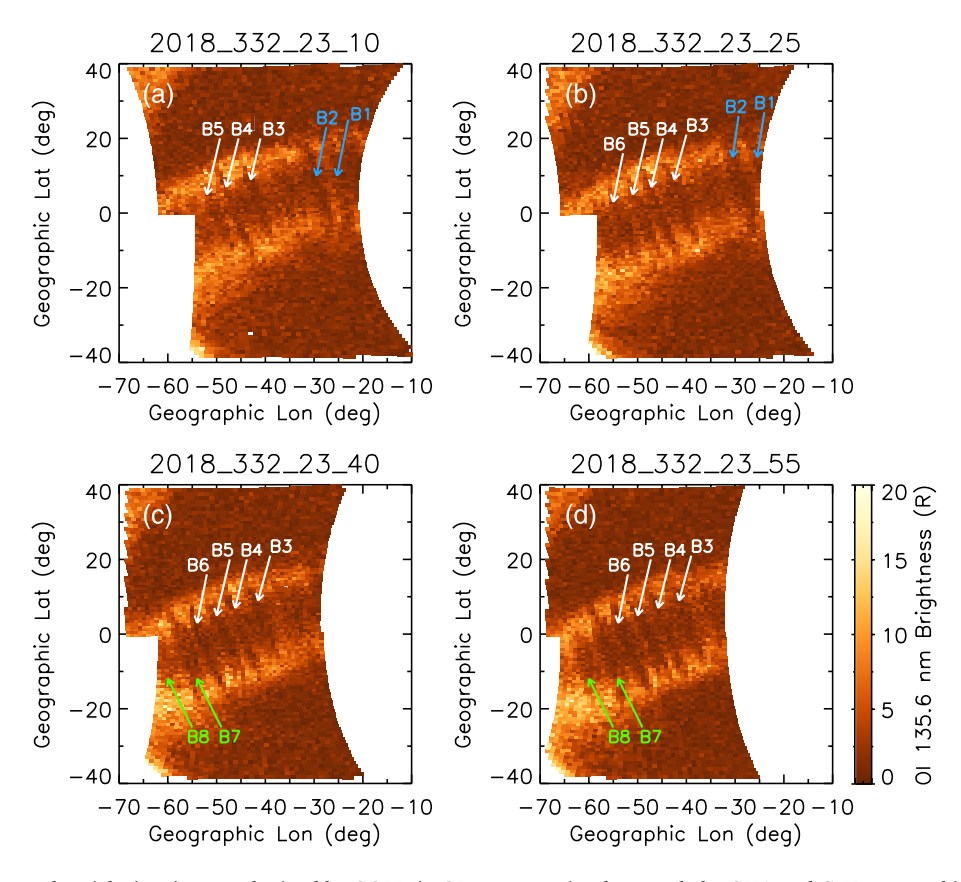


Figure 1. The nighttime images obtained by GOLD in OI 135.6 nm simultaneously by CHA and CHB are combined on 28 November 2018. (a–d) Obtained at 23:10, 23:25, 23:40, and 23:55 UT, respectively. The observed longitude region gradually moves westward with time. The two bright emission patches seen at all longitudes are the crests of the EIA. Depletions in the brightness across the EIA crests, known as equatorial plasma bubbles (EPBs), are seen. Multiple EPBs are observed in this longitude range.

images from east to west longitudes. Hence, the observed longitudes within this 1 hr have shifted west. Because of this, EPBs (marked by blue arrows) on the eastern boundary (around 25°W) of the images at 23:10 UT (Figure 1a) and 23:25 UT (Figure 1b) are not observed at 23:40 UT (Figure 1c) and 23:55 UT (Figure 1d). On the other hand, some EPBs (marked by green arrows) appear around 55°W only in the images obtained at 23:40 (Figure 1c) and 23:55 UT (Figure 1d). However, EPBs shown by white arrows are observed at all four times (except B6, which is out of the observed region at 23:10 UT). Supporting information Figures S1 and S2 show the night images obtained by GOLD on 27 and 29 November 2018 in the similar way as Figure 1.

The quasi dipole (QD) geomagnetic coordinates (Richmond, 1995) at 300 km altitude (the assumed altitude of the emission) corresponding to geographic coordinates are calculated from the IGRF 2018 scalar potentials (Thébault et al., 2015). Applying this coordinate transformation to the images in Figures 1a–1d gives the images shown in Figures 2a, 2c, 2e, and 2g. Both EIA crests are located near $\pm 12^{\circ}$ MLAT and EPBs are aligned along the magnetic longitudes.

Three different magnetic latitude regions of $(5^{\circ} \text{ to } 15^{\circ})$, $(-5^{\circ} \text{ to } 5^{\circ})$, and $(-15^{\circ} \text{ to } -5^{\circ})$ between 20° and 35° MLON are selected, which are shown by green, blue, and magenta boxes, respectively in Figures 2a, 2c, 2e, and 2f. The latitude ranges are selected to distinguish both the EIA crests from the magnetic equatorial region. The green and magenta boxes cover the north (N) and south (S) EIA crests. The blue boxes cover the magnetic equatorial latitudes. The sample magnetic longitude range $(20^{\circ} \text{ to } 35^{\circ})$ is selected since it is observed in all four images and multiple EPBs are present within this range. The brightness along the latitudes in each box is summed. Since the resolution along the magnetic longitude is 0.5° , the summed brightness is smoothed over 1° longitude to decrease the uncertainties in determining the minima positions. Variations of the smoothed brightness in each box along the magnetic longitudes are shown as lines with

KARAN ET AL. 4 of 11

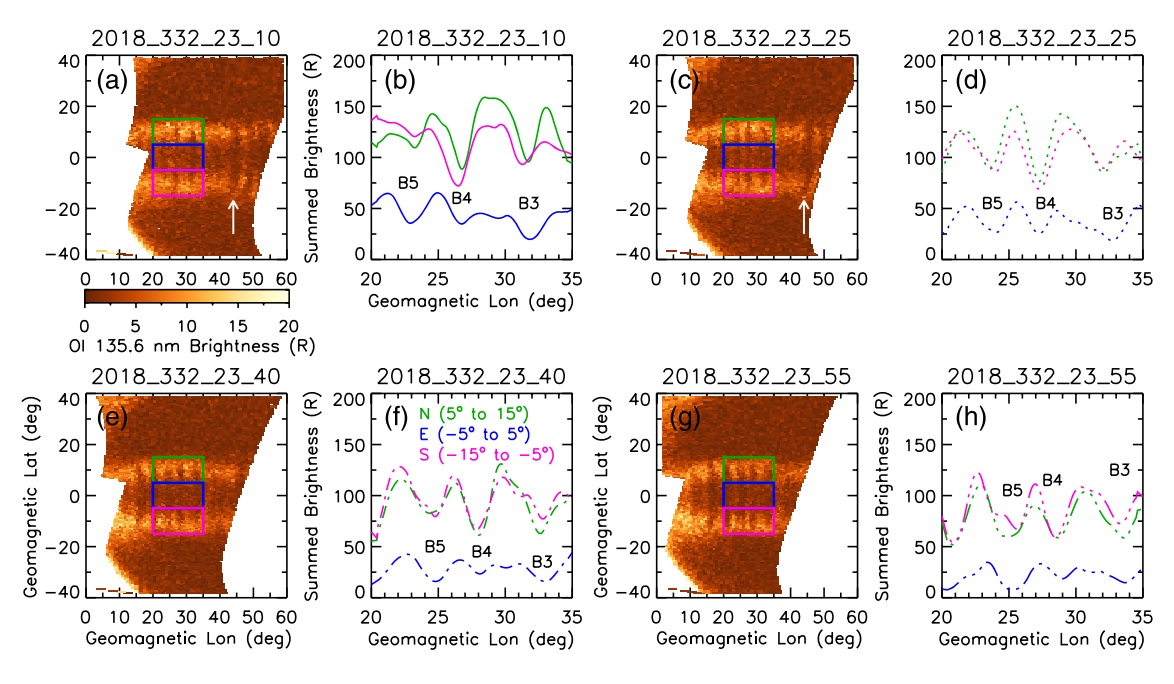


Figure 2. (a, c, e, and g) The nighttime images observed by GOLD in geomagnetic coordinates corresponding to the images shown in Figures 1a–1d. The green, blue, and magenta boxes are the regions selected at the N crest, magnetic equator, and S crest of EIA latitudes (common on each panel), respectively. The brightness within each box is summed along the latitudes and their variation along the longitudes are shown with the corresponding colors in (b), (d), (f), and (h). Three EPBs are observed in the selected longitude region. Variations of the summed brightness along longitudes at different times are shown by different line styles.

corresponding colors in Figures 2b, 2d, 2f, and 2h, respectively. Different line styles in Figures 2b, 2d, 2f, and 2h correspond to different times. The dips in the integrated smoothed brightness are due to EPBs in the selected regions. Three EPBs (B5, B4, and B3) can be observed in the selected geomagnetic longitude range. The magnetic longitudes of (B5, B4, and B3) at the N crest EIA region are (23.2°, 26.8°, and 31.7°), (23.6°, 27.2°, and 32.1°), (24.3°, 28°, and 32.6°), and (25°, 28.7°, and 33.6°) at 23:10, 23:25, 23:40, and 23:55, respectively. Magnetic longitudes of (B5, B4, and B3) at the magnetic equatorial region are (23°, 26.7°, and 31.9°), (24.1°, 27.2°, and 32.7°), (24.8°, 28.1°, and 33°), and (25.3°, 29°, and 33.6°) at 23:10, 23:25, 23:40, and 23:55, respectively. Similarly, the magnetic longitudes of (B5, B4, and B3) at the S crest EIA region are (23.2°, 26.4°, and 31.3°), (24°, 27.2°, and 32.1°), (24.7°, 27.9°, and 32.8°), and (25.6°, 28.4°, and 33.3°) at 23:10, 23:25, 23:40, and 23:55, respectively. From the magnetic longitudes of B5, B4, and B3, it can be noted that at all latitude regions EPBs are moving east.

To clearly see the movements of EPBs, the summed, smoothed brightness obtained at all four times (Figures 2b, 2d, 2f, and 2h) are overplotted in Figures 3a, 3c, and 3e for N crest of EIA, magnetic equator, and S crest of EIA, respectively. Three arrows are drawn for guidance to mark the broad drifting of EPBs. Notice the gradual decrease of brightness with time at each latitude region. This is understood to be caused by decrease in plasma densities due to radiative recombination process. Magnetic longitudes of individual EPBs at the four different observation times (i.e., 23:10, 23:25, 23:40, and 23:55 UT) are shown in Figures 3b, 3d, and 3f corresponding to Figures 3a, 3c, and 3e, respectively. The positive slope of each line indicates the eastward zonal drift of EPBs. It is also noted that for individual EPBs the amount of longitudinal shift varies with time. The line slopes at different latitude regions are similar.

The method of analysis as explained above has been carried out with the nighttime data obtained on 27-29 November 2018. Magnetic longitudes of the EPBs on these three nights are shown in Figures 4a–4c, respectively. These are geomagnetic quiet periods. The horizontal axes show the times of observation and the vertical axes show the geomagnetic longitude locations of the observed EPBs. Here the entire observed longitude range is considered without taking a sample longitude range (as in Figure 2). EPBs whose locations are available a minimum of three times are considered. The locations of the EPBs at the N crest, magnetic equator, and S crest are independently obtained. The total numbers of EPBs considered on 27-29 November 2018 are 8, 4, and 6, respectively. On 27 and 29 November 2018, EPBs are spread across the

KARAN ET AL. 5 of 11

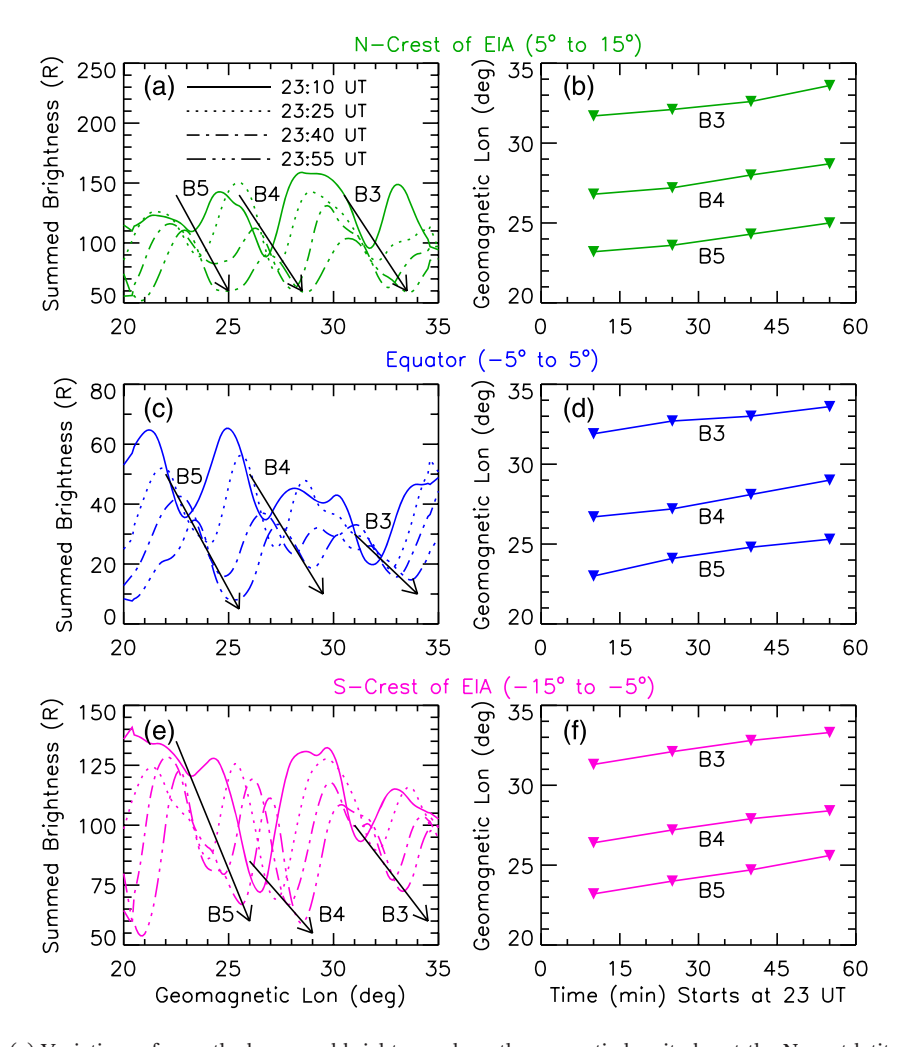


Figure 3. (a) Variations of smoothed summed brightness along the magnetic longitudes at the N crest latitudes of the EIA at 23:10 (solid), 23:25 (dotted), 23:40 (dash-dot-dash), and 23:55 UT (dash-double dot-dash) UT as shown in Figures 2b, 2d, 2f, and 2h. (c and e) Similar to (a) but at magnetic equator and S crest latitudes of the EIA. Figures 3a, 3c, and 3e compare the longitudinal shift of EPBs at four different times. (b, d, and f) The magnetic longitudes at the four times for individual EPBs as shown in (a), (c), and (e).

entire longitude range of observation. However, on 28 November 2018, no EPBs are seen in the \sim 35° to 45° longitude range (Figure 4b). This could be due to either the variations in the ionospheric electric fields or in the background thermosphere within the considered longitude range or both. This shows a day-to-day variability of EPB occurrence which will be investigated in detail in future work.

On 27–29 November 2018, the distances between adjacent EPBs are calculated at both the EIA-crest regions and the magnetic equator. The same spatial separation is observed at the three locations. On 27–29 November 2018, the average spacing between adjacent EPBs is \sim 377, 526, and 442 km, respectively, and their minimum separation is \sim 3° longitude. In the lower thermosphere, the neutral zonal wind shows small-scale spatial variations which, in turn, can create gravity waves (GWs) with horizontal scales between 50 and 300 km (e.g., Karan & Pallamraju, 2017; Stober et al., 2018). These GWs are one of the potential candidates for the seeding mechanism of the nighttime plasma irregularities (Cai et al., 2014; Takahashi et al., 2009; Tsunoda, 2010) and may produce the EPBs at a separation of \sim 3° longitude.

From the geomagnetic longitudes at four or three times, three or two zonal drift velocities of EPBs can be calculated. While deriving drift velocities, distances between EPBs are calculated in geographic coordinates. For individual EPBs, the changes in location (Figure 4) at every 15 min observation are similar through the hour. Thus, an average drift velocity is calculated for each EPB. The standard error of the average drift velocity is obtained by dividing the 1σ statistical standard deviation by the square root of the number of

KARAN ET AL. 6 of 11

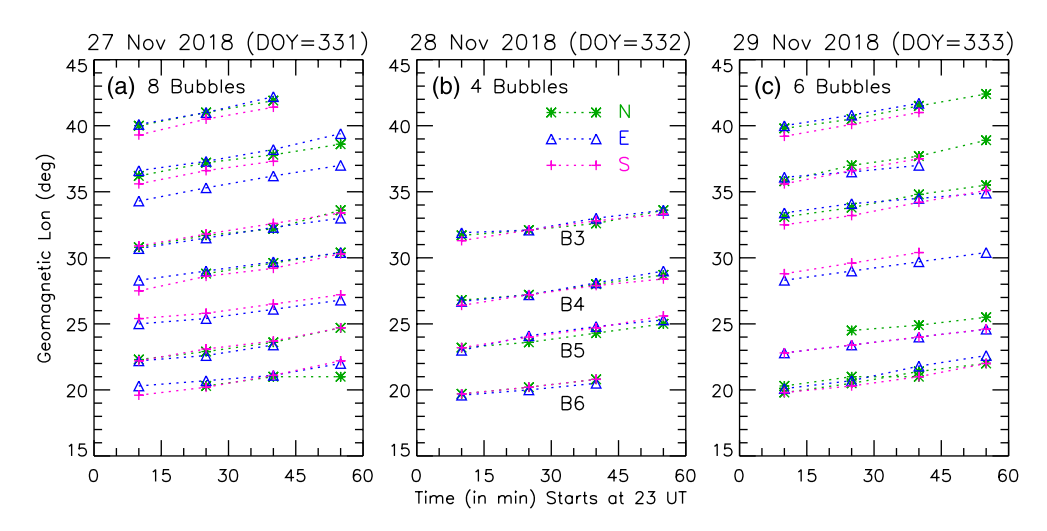


Figure 4. (a–c) The magnetic longitudes of EPBs (observed within 15° to 45° magnetic longitudes) at the four observation times on 27–29 November 2018, respectively. Magnetic longitudes of individual EPBs at the N crest of EIA, magnetic equator, and S crest of EIA are shown by star, triangle, and plus symbols, respectively.

observations. Since the average drift velocity and the standard error for individual EPBs are calculated from only 2 or 3 drift velocities, the spread in the standard error values is large. Figures 5a-5c show the calculated average drift velocities of EPBs with their standard error on 27-29 November 2018, respectively. The horizontal axes show the longitudes (both geomagnetic and geographic) and the vertical axes show the drift velocities of the EPBs. Longitude of an EPB in the figure is the average of longitudes of that EPB at all times. The drift velocities of EPBs at the N crest, magnetic equator, and S crest latitudes of EIA are marked by star, triangle, and plus symbols, respectively. EPBs whose drift velocities are calculated only at one or two latitude regions are marked by circles. Occasionally, due to low OI 135.6 nm emission brightness at some pixels, determining the location of EPBs becomes difficult, and hence, the drift velocities are not calculated (for example, N crest of the EPB at 29° MLON in Figure 5a and equatorial region of the EPBs whose drift velocities are marked by circles in Figure 5c). In Figure 5a, a drift velocity of the EPB at 35.5° MLON (marked by a circle) is available only at the equatorial latitudes, since the EPB is extended only at this latitude range. On these 3 days the drift velocities at all the latitudes are similar for almost all the EPBs. However, there are a few exceptions. On 27 November 2018, EPBs observed at 21°, 23°, 29°, and 32° MLON (Figure 5a) have lower drift velocities at the magnetic equator than at the EIA crests. On that day the drift velocities at the magnetic equator gradually increase with longitudes from west to east. The average drift velocities of EPBs on 27-29 November 2018 are found to be 116 + 4, 80 ± 3 , and 107 ± 10 m/s, respectively, at the N crest; 105 ± 9 , 88 ± 11 , and 110 ± 4 m/s, respectively, at the magnetic equator and 118 ± 6 , 95 ± 7 , and 106 ± 8 m/s, respectively, at the S crest. The drift velocities of all EPBs observed on the 3 days are summarized in Table 1.

4. Discussion

The first measurement of zonal drift velocities of EPBs observed from geostationary orbit by GOLD is obtained. There have been many previous reports on zonal drift velocities of EPBs from both ground and space observations. Investigators using all-sky imager (ASI) data have reported drift velocities of ~80–190 m/s (Mendillo & Baumgardner, 1982), ~20–100 m/s (Mendillo et al., 1997), ~80–100 m/s (Taylor et al., 1997), ~40–190 m/s (Sinha & Raizada, 2000), ~60–160 m/s (Pimenta et al., 2001), ~40–150 m/s (Martinis et al., 2003), ~90–120 m/s (Chapagain et al., 2012), ~100–180 m/s (Hickey et al., 2018), and ~40–120 m/s (Gurav et al., 2019). With the resolution of GOLD and nighttime SNR of measured OI 135.6 nm brightness, the derived drift velocities ~60–145 m/s match well with the previously reported values. The measurements from IMAGE-FUV, taken during high solar activity were higher: 80–170 m/s (e.g., England & Immel, 2012).

Different patterns in the latitudinal variations of EPB zonal drift velocities have been reported in the published literature. Dynamics Explorer 2 satellite measurements showed that the eastward plasma drifts at

KARAN ET AL. 7 of 11

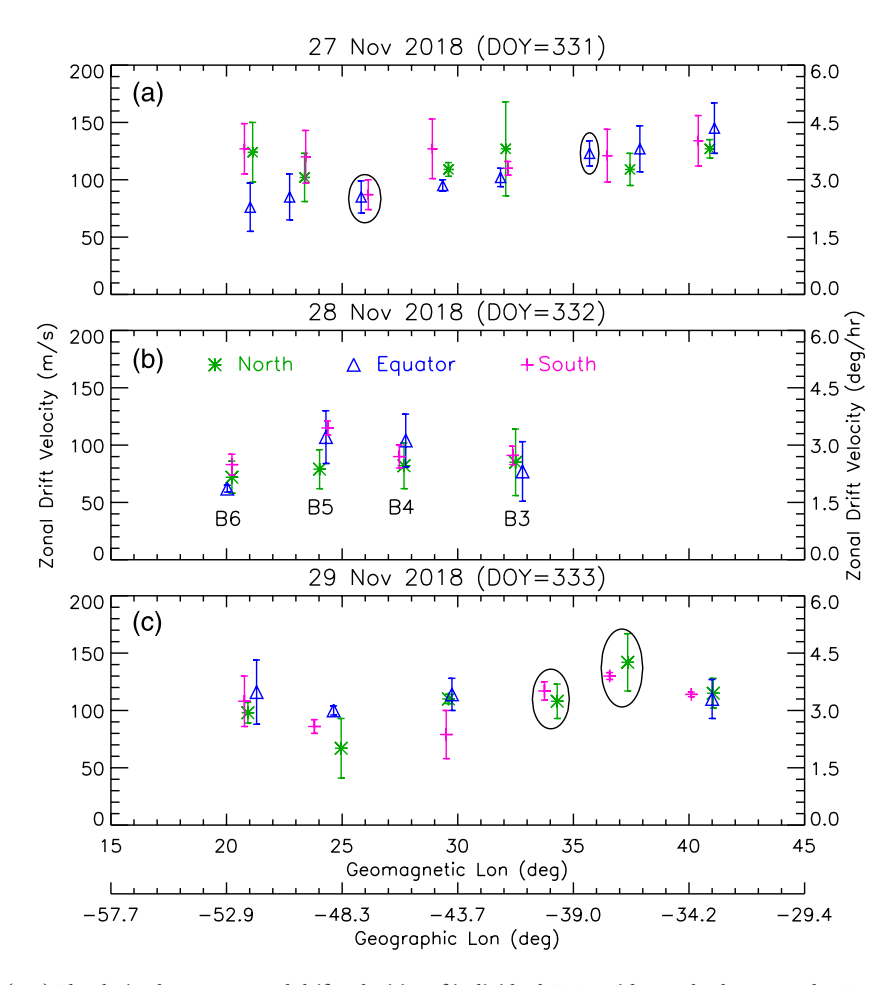


Figure 5. (a–c) The derived average zonal drift velocities of individual EPBs with standard error at the N crest, equator, and S crest on 27–29 November 2018, respectively. The right *Y* axis shows the average drift velocities in magnetic longitude degrees per hour. For the EPBs whose drift velocities are circled, velocities are not available at all latitudes.

the magnetic equator are smaller than the ones at off-equatorial latitudes (\sim 26° dip latitude) after 20:00 LT during high solar activity period (Aggson et al., 1987; Coley & Heelis, 1989). This was attributed to an altitude dependence of the F region dynamo electric field. Monthly average drift velocities of plasma irregularities that cause scintillation of radio signals near the EIA S crest latitudes are reported to be lower than the velocity at the geomagnetic equatorial region (Basu et al., 1996; Kil et al., 2002). This decrease is attributed to a larger neutral-ion drag force due to the higher ion densities. From ground-based nightglow measurements, eastward plasma drifts over magnetic equator are observed to be smaller than at the EIA

Table 1	
Summary of the Calculated Zonal Dri	ift Velocities (m/s) of EPBs

		EPB zonal drift velocities (m/s)							
Date	Latitudes	B8	В7	В6	В5	B4	В3	B2	B1
27 Nov 2018	N (5° to 15°)	124 ± 26	102 ± 21		109 ± 5	127 ± 41		109 ± 15	127 ± 8
	$E(-5^{\circ} \text{ to } 5^{\circ})$	76 ± 21	85 ± 20	85 ± 14	95 ± 5	102 ± 8	123 ± 11	127 ± 20	145 ± 22
	$S (-15^{\circ} \text{ to } -5^{\circ})$	127 ± 22	120 ± 23	87 ± 13	127 ± 26	110 ± 6		121 ± 23	134 ± 22
28 Nov 2018	N (5° to 15°)			72 ± 14	79 ± 17	82 ± 20	85 ± 29		
	$E(-5^{\circ} \text{ to } 5^{\circ})$			62 ± 3	107 ± 23	104 ± 23	77 ± 26		
	$S (-15^{\circ} \text{ to } -5^{\circ})$			83 ± 9	115 ± 6	90 ± 10	91 ± 8		
29 Nov 2018	N (5° to 15°)			98 ± 9	67 ± 26	110 ± 4	108 ± 15	142 ± 25	115 ± 13
	$E(-5^{\circ} \text{ to } 5^{\circ})$			116 ± 28	100 ± 4	114 ± 14			110 ± 17
	$S(-15^{\circ} \text{ to } -5^{\circ})$			108 ± 22	86 ± 6	79 ± 21	117 ± 8	130 ± 3	114 ± 3

KARAN ET AL. 8 of 11



crest latitudes (~16°S MLAT) during postsunset hours while the pattern reversed during postmidnight hours (Martinis et al., 2003). The smaller drifts near the magnetic equator during postsunset hours are due to the influence of E region dynamo, whereas the postmidnight pattern is due to the decreasing eastward plasma drifts above the F peak (Anderson & Mendillo, 1983). Using FUV emission measurements from the IMAGE satellite during high solar activity period, the depletion drift velocities are observed to be similar at 4-10° MLAT but decrease at 12-18° MLAT after 22:00 magnetic local time (England & Immel, 2012; Liu et al., 2013). Thus, in most studies, similar drift velocities are reported for ~0-12° MLAT. Further, the drift velocities decrease beyond this latitude during high solar activity period. In the present study, the drift velocities of EPBs at the three latitude regions are obtained at ~19-22 LT during a low solar activity period and the EIA crests are near 12° MLAT, so the observed similarities in the drift velocities at the three latitudes are reasonable. Out of the 18 EPBs observed, only four have lower drift velocities at the magnetic equator than at the EIA crests which is consistent with the published reports (e.g., Anderson & Mendillo, 1983; Basu et al., 1996; Kil et al., 2002; Martinis et al., 2003). Since EPBs are common in GOLD observations, the present investigation provides a baseline for future statistical studies of EPBs. A longer-term systematic investigation of the drift velocities is planned to improve the statistics and provide a clearer understanding of how the drift velocities vary with latitude and season.

Latitudinal differences in the zonal drift velocities is expected to cause a westward tilt in the structure of EPBs (Anderson & Mendillo, 1983; Kil et al., 2002; Martinis et al., 2003; Pimenta et al., 2003). In the present study, some differences in the structure of the EPBs are seen in the EIA crest regions. In Figures 2a and 2c, EPBs indicated by an arrow seem to be stretched toward the western longitudes at the S crest of the EIA. In Figure 4a, notice the location of the EPB (at $\sim 37.5^{\circ}$ MLON) at the three latitude regions in all times. At the S crest of the EIA, the EPB curves westward. Detailed investigation of these EPBs will give insights into their different shapes. Nevertheless, it is also necessary to consider that the viewing angle to EPBs along with the curvature of the magnetic field lines at different altitudes, may contribute to the change in the shape (Eastes et al., 2019).

In the present work, we have focused on a fixed longitude region (65°W to 20°W) near the subsatellite point. As GOLD makes observations also over the Atlantic and west African longitudes, a similar investigation at those longitude regions is planned. This will give us information on the variation of EPB zonal drift velocities at different longitudes. The data from ICON (Ionospheric Connection Explorer) and COSMIC-2 satellites will be useful for these studies.

5. Summary

The OI 135.6 nm images obtained by GOLD on three consecutive and geomagnetically quiet nights are investigated. For each night, a sequence of four images with simultaneous observations from both the Northern and Southern Hemispheres are examined for EPBs. Multiple EPBs are observed in each image on every day. As EPBs are aligned along the magnetic field, they are resampled in geomagnetic coordinates. Three different latitude regions (north and south crests of the EIA and magnetic equator) are selected. At each latitude region, using the longitudinal shift of EPBs in every 15 min, the zonal drift velocities are calculated. For each EPBs, all the calculated drift velocities in 1 hr are averaged to find the average drift velocity with its standard error. Averaging all the EPB drift velocities on each day, on 27-29 November 2018, the drift velocities are found to be, respectively, 116 ± 4 , 80 ± 3 , and 107 ± 10 m/s at the North crest, 105 ± 9 , 88 ± 11 , and 110 ± 4 m/s at the magnetic equator, and 118 ± 6 , 95 ± 7 , and 106 ± 8 m/s at the South crest of the EIA. The drift velocities at the EIA crests and the equator are the same within their standard error. Thus, the present study reports the derivation of drift velocities of EPBs observed by GOLD from geostationary orbit. For the first time, simultaneous measurement of EPBs drift velocities at both crests of the EIA and the equator is obtained. EPBs are very common in GOLD observations, thus can be used for more extensive future studies. Similar investigations for a longer period of time and at other longitudes observed by GOLD will give more insights to the understanding of ionospheric plasma irregularities.

Data Availability Statement

The GOLD data are available from the GOLD Science Data Center (http://gold.cs.ucf.edu/search/) and NASA's Space Physics Data Facility (https://spdf.gsfc.nasa.gov).

KARAN ET AL. 9 of 11



Acknowledgments

The principal author thanks Wenbin Wang for his useful discussions. This research was supported by NASA contract 80GSFC18C0061 to the University of Colorado.

References

- Aa, E., Zou, S., Eastes, R., Karan, D. K., Zhang, S.-R., Erickson, P. J., & Coster, A. J. (2020). Coordinated ground-based and space-based observations of equatorial plasma bubbles. *Journal of Geophysical Research: Space Physics*, 125, e2019JA027569. https://doi.org/10.1029/ 2019JA027569
- Abdu, M. A., Batista, I. S., Sobral, J. H. A., de Paula, E. R., & Kantor, I. J. (1985). Equatorial ionospheric plasma bubble irregularity occurrence and zonal velocities under quiet and disturbed conditions, from Polarimeter observations. *Journal of Geophysical Research*, 90(A10), 9921–9928. https://doi.org/10.1029/JA090iA10p09921
- Abdu, M. A., Bittencourt, J. A., & Batista, I. S. (1981). Magnetic declination control of the equatorial F-region dynamo electric field development and spread-F. Journal of Geophysical Research, 86, 11,443–11,446. https://doi.org/10.1029/JA086iA13p11443
- Aggson, T. L., Maynard, N. C., Herrero, F. A., Mayr, H. G., Brace, L. H., & Liebrecht, M. C. (1987). Geomagnetic equatorial anomaly in zonal plasma flow. *Journal of Geophysical Research*, 92(A1), 311–315. https://doi.org/10.1029/JA092iA01p00311
- Anderson, D. N., & Mendillo, M. (1983). Ionospheric conditions affecting the evolution of equatorial plasma depletions. *Geophysical Research Letters*, 10, 541–544. https://doi.org/10.1029/GL010i007p00541
- Basu, S., Kudeki, E., Basu, S., Valladares, C. E., Weber, E. J., Zengingonul, H. P., et al. (1996). Scintillations, plasma drifts, and neutral winds in the equatorial ionosphere after sunset. *Journal of Geophysical Research*, 101(A12), 26,795–26,809. https://doi.org/10.1029/96JA00760
- Burke, W. J., Gentile, L. C., Huang, C. Y., Valladares, C. E., & Su, S. Y. (2004). Longitudinal variability of equatorial plasma bubbles observed by DMSP and ROCSAT-1. *Journal of Geophysical Research*, 109. https://doi.org/10.1029/2004JA010583
- Cai, X., Burns, A. G., Wang, W., Coster, A., Qian, L., Liu, J., et al. (2020). Comparison of GOLD nighttime measurements with total electron content: preliminary results. *Journal of Geophysical Research: Space Physics*, 125. https://doi.org/10.1029/2019JA027767
- Cai, X., Yuan, T., Zhao, Y., Pautet, P.-D., Taylor, M. J., & Pendleton, W. R. (2014). A coordinated investigation of the gravity wave breaking and the associated dynamical instability by a Na lidar and an advanced mesosphere temperature mapper over Logan, UT (41.7°N, 111.8°W). *Journal of Geophysical Research: Space Physics*, 119, 6852–6864. https://doi.org/10.1002/2014JA020131
- Chapagain, N. P., Taylor, M. J., Makela, J. J., & Duly, T. M. (2012). Equatorial plasma bubble zonal velocity using 630.0 nm airglow observations and plasma drift modeling over Ascension Island. *Journal of Geophysical Research*, 117, A06316. https://doi.org/10.1029/2012JA017750
- Coley, W. R., & Heelis, R. A. (1989). Low-latitude zonal and vertical ion drifts seen by DE 2. *Journal of Geophysical Research*, 94(A6), 6751–6761. https://doi.org/10.1029/JA094iA06p06751
- Eastes, R. W., McClintock, W. E., Burns, A. G., Anderson, D. N., Andersson, L., Aryal, S., et al. (2020). Initial Observations by the Global-scale Observations of the Limb and Disk (GOLD) mission. *Journal of Geophysical Research: Space Physics*, 125, e2020JA027823. https://doi.org/10.1029/2020JA027823
- Eastes, R. W., McClintock, W. E., Burns, A. G., Anderson, D. N., Anderson, L., Codrescu, M., et al. (2017). The Global-Scale Observations of the Limb and Disk (GOLD) Mission. Space Science Reviews, 212(1-2), 383-408. https://doi.org/10.1007/s11214-017-0392-2
- Eastes, R. W., Solomon, S. C., Daniell, R. E., Anderson, D. N., Burns, A. G., England, S. L., et al. (2019). Global-scale observations of the equatorial ionization anomaly. *Geophysical Research Letters*, 46, 9318–9326. https://doi.org/10.1029/2019GL084199
- England, S. L., & Immel, T. J. (2012). An empirical model of the drift velocity of equatorial plasma depletions. *Journal of Geophysical Research*, 117, A12308. https://doi.org/10.1029/2012JA018091
- Fejer, B. G., & Kelley, M. C. (1980). Ionospheric irregularities. *Reviews of Geophysics*, 18(2), 401–454. https://doi.org/10.1029/RG018i002p00401
- Gurav, O. B., Narayanan, V. L., Sharma, A. K., Ghodpage, R. N., Gaikwad, H. P., & Patil, P. T. (2019). Airglow imaging observations of some evolutionary aspects of equatorial plasma bubbles from Indian sector. *Advances in Space Research*, 64, 385–399. https://doi.org/10.1016/i.asr.2019.04.008
- Henderson, S. B., Swenson, C. M., Christensen, A. B., & Paxton, L. J. (2005). Morphology of the equatorial anomaly and equatorial plasma bubbles using image subspace analysis of global ultraviolet imager data. *Journal of Geophysical Research*, 110, A11306. https://doi.org/ 10.1029/2005JA011080
- Hickey, D. A., Martinis, C. R., Mendillo, M., Baumgardner, J., Wroten, J., & Milla, M. (2018). Simultaneous 6300 Å airglow and radar observations of ionospheric irregularities and dynamics at the geomagnetic equator. *Annales de Geophysique*, 36, 473–487. https://doi.org/10.5194/angeo-36-473-2018
- Huang, C.-S., de La Beaujardiere, O., Roddy, P. A., Hunton, D. E., Pfaff, R. F., Valladares, C. E., & Ballenthin, J. O. (2011). Evolution of equatorial ionospheric plasma bubbles and formation of broad plasma depletions measured by the C/NOFS satellite during deep solar minimum. *Journal of Geophysical Research*, 116, A03309. https://doi.org/10.1029/2010JA015982
- Huba, J. D., & Joyce, G. (2007). Equatorial spread F modeling: Multiple bifurcated structures, secondary instabilities, large density "bite-outs", and supersonic flows. Geophysical Research Letters, 34, L07105. https://doi.org/10.1029/2006GL028519
- Huba, J. D., & Liu, H.-L. (2020). Global modeling of equatorial spread F with SAMI3/WACCM-X. Geophysical Research Letters, 47. https://doi.org/10.1029/2020GL088258
- Huba, J. D., Wu, T.-W., & Makela, J. J. (2015). Electrostatic reconnection in the ionosphere. *Geophysical Research Letters*, 42, 1626–1631. https://doi.org/10.1002/2015GL063187
- Immel, T. J., Mende, S. B., Frey, H. U., Peticolas, L. M., & Sagawa, E. (2003). Determination of low latitude plasma drift speeds from FUV images. Geophysical Research Letters, 30(18). https://doi.org/10.1029/2003GL017573
- Karan, D. K., & Pallamraju, D. (2017). Small-scale longitudinal variations in the daytime equatorial thermospheric wave dynamics as inferred from oxygen dayglow emissions. *Journal of Geophysical Research: Space Physics*, 122, 6528–6542. https://doi.org/10.1002/ 2017JA023891
- Karan, D. K., & Pallamraju, D. (2020). On estimation of daytime equatorial vertical (E × B) plasma drifts using optical neutral dayglow emission measurements. *Journal of Geophysical Research: Space Physics*, 125, e2019JA026775. https://doi.org/10.1029/2019JA026775
- Karan, D. K., Pallamraju, D., Phadke, K. A., Vijayalakshmi, T., Pant, T. K., & Mukherjee, S. (2016). Electrodynamic influence on the diurnal behavior of neutral daytime airglow emissions. *Annales de Geophysique*, 34, 1019–1030. https://doi.org/10.5194/angeo-34-1019-2016
- Kelley, M. C. (2009). Equatorial plasma instabilities and mesospheric turbulence. In *The Earth's ionosphere: Plasma physics and electrodynamics* (2nd ed., pp. 142–149). MA, USA: Academic Press.
- Kepkar, A., Arras, C., Wickert, J., Schuh, H., Alizadeh, M., & Tsai, L.-C. (2019). Global climatology of equatorial plasma bubbles based on GPS radio occultation from FormoSat-3/COSMIC. *Annual Geophysical Discussion*. https://doi.org/10.5194/angeo-2019-45
- Kil, H., Kintner, P. M., de Paula, E. R., & Kantor, I. J. (2002). Latitudinal variations of scintillation activity and zonal plasma drifts in South America. *Radio Science*, 37(1). https://doi.org/10.1029/2001RS002468

KARAN ET AL. 10 of 11



- Liu, G., England, S. L., Frey, H. U., Immel, T. J., Lin, C. S., Pacheco, E. E., et al. (2013). Comparison of drift velocities of nighttime equatorial plasma depletions with ambient plasma drifts and thermospheric neutral winds. *Journal of Geophysical Research: Space Physics*, 118, 7360–7368. https://doi.org/10.1002/2013JA019329
- Makela, J. J. (2006). A review of imaging low-latitude ionospheric irregularity processes. Journal of Atmospheric and Solar-Terrestrial Physics, 68(13), 1441–1458. https://doi.org/10.1016/j.jastp.2005.04.014
- Mandal, S., Pallamraju, D., Karan, D. K., Phadke, K. A., Singh, R. P., & Suryawanshi, P. (2019). On deriving gravity wave characteristics in the daytime upper atmosphere using radio technique. *Journal of Geophysical Research: Space Physics*, 124, 6985–6997. https://doi.org/ 10.1029/2019JA026723
- Martinis, C., Eccles, J. V., Baumgardner, J., Manzano, J., & Mendillo, M. (2003). Latitude dependence of zonal plasma drifts obtained from dual-site airglow observations. *Journal of Geophysical Research*, 108(A3), 1129. https://doi.org/10.1029/2002JA009462
- McClintock, W. E., Eastes, R. W., Beland, S., Bryant, K. B., Burns, A. G., Correira, J., et al. (2020). Global-scale measurements of the Limb and Disk (GOLD) mission implementation: 2. Observations, data pipeline and level 1 data products. *Journal of Geophysical Research:* Space Physics, 125, e2020JA027809. https://doi.org/10.1029/2020JA027809
- Mendillo, M., & Baumgardner, J. (1982). Airglow characteristics of equatorial plasma depletions. *Journal of Geophysical Research*, 87(A9), 7641–7652. https://doi.org/10.1029/JA087iA09p07641
- Mendillo, M., Baumgardner, J., Colerico, M., & Nottingham, D. (1997). Imaging science contributions to equatorial aeronomy: Initial results from the MISETA program. *Journal of Atmospheric and Solar Terrestrial Physics*, 59, 1587–1599. https://doi.org/10.1016/s1364-6826(96)00158-7
- Mendillo, M., & Tyler, A. (1983). Geometry of depleted plasma regions in the equatorial ionosphere. *Journal of Geophysical Research*, 88(A7), 5778–5782. https://doi.org/10.1029/JA088iA07p05778
- Narayanan, V. L., Gurubaran, S., Shiny, M. B. B., Emperumal, K., & Patil, P. T. (2017). Some new insights of the characteristics of equatorial plasma bubbles obtained from Indian region. *Journal of Atmospheric and Solar Terrestrial Physics*, 156(2017), 80–86. https://doi.org/10.1016/j.jastp.2017.03.006
- Pallamraju, D., Chakrabarti, S., & Valladares, C. E. (2004). Magnetic storm-induced enhancement in neutral composition at low latitudes as inferred by O(1D) dayglow measurements from Chile. *Annales de Geophysique*, 22, 3241–3250. https://doi.org/10.5194/angeo-22-3241-2004
- Pallamraju, D., Karan, D. K., & Phadke, K. A. (2016). First three-dimensional wave characteristics in the daytime upper atmosphere derived from ground-based multiwavelength oxygen dayglow emission measurements. *Geophysical Research Letters*, 42. https://doi.org/10.1002/2016GL069074
- Park, S. H., England, S. L., Immel, T. J., Frey, H. U., & Mende, S. B. (2007). A method for determining the drift velocity of plasma depletions in the equatorial ionosphere using far-ultraviolet spacecraft observations. *Journal of Geophysical Research*, 112. https://doi.org/10.1029/2007JA012327
- Pimenta, A. A., Fagundes, P. R., Bittencourt, J. A., Sahai, Y., Gobbi, D., Medeiros, A. F., & Taylor, M. J. (2001). Ionospheric plasma bubble zonal drift: A methodology using OI 630 nm all-sky Imaging systems. *Advances in Space Research*, 27(2001), 1219–1224. https://doi.org/10.1016/S0273-1177(01)00201-0
- Pimenta, A. A., Fagundes, P. R., Sahai, Y., Bittencourt, J. A., & Abalde, J. R. (2003). Equatorial F-region plasma depletion drifts: Latitudinal and seasonal variations. Annales Geophysicae, 21, 2315–2322. https://doi.org/10.5194/angeo-21-2315-2003
- Rajesh, P. K., Lin, C. H., Chen, C. H., Chen, W. H., Lin, J. T., Chou, M. Y., et al. (2017). Global equatorial plasma bubble growth rates using ionosphere data assimilation. *Journal of Geophysical Research: Space Physics*, 122, 3777–3787. https://doi.org/10.1002/2017JA023968
- Richmond, A. D. (1995). Ionospheric electrodynamics using magnetic apex coordinates. *Journal of Geomagnetism and Geoelectricity*, 47, 191–212. https://doi.org/10.5636/jgg.47.191
- Sahai, Y., Aarons, J., Mendillo, M., Baumgardner, J., Bittencourt, J., & Takahasi, H. (1994). OI 630 nm imaging observations of equatorial plasma depletions at 16° dip latitude. *Journal of Atmospheric and Solar Terrestrial Physics*, 56, 1461–1475. https://doi.org/10.1016/0021-9169(94)90113-9
- Sekar, R. (2003). Plasma instabilities and their simulations in the equatorial F region Recent results. Space Science Reviews, 107, 251–262. https://doi.org/10.1023/A:1025592226703
- Shiokawa, K., Otsuka, Y., Lynn, K. J., Wilkinson, P., & Tsugawa, T. (2015). Airglow-imaging observation of plasma bubble disappearance at geomagnetically conjugate points. *Earth, Planets and Space*, 67(1), 1–12. https://doi.org/10.1186/s40623-015-0202-6
- Shiokawa, K., Otsuka, Y., Ogawa, T., & Wilkinson, P. (2004). Time evolution of high-altitude plasma bubbles imaged at geomagnetic conjugate points. *Annales de Geophysique*, 22, 3137–3143. https://doi.org/10.5194/angeo-22-3137-2004
- Sinha, H. S. S., & Raizada, S. (2000). Some new features of ionospheric plasma depletions over the Indian zone using all sky optical imaging. Earth, Planets and Space, 52(8), 549–559. https://doi.org/10.1186/BF03351662
- Sobral, J., & Abdu, M. (1991). Solar activity effects on equatorial plasma bubble zonal velocity and its latitude gradient as measured by airglow scanning photometers. *Journal of Atmospheric and Solar Terrestrial Physics*, 53, 729–742. https://doi.org/10.1016/0021-0160(01)00134.px
- Sridharan, R., Pallam Raju, D., & Raghavarao, R. (1994). Precursor to equatorial spread-F in OI 630.0 nm dayglow. *Journal of Geophysical Research*, 21(25), 2797–2800. https://doi.org/10.1029/94GL02732
- Stober, G., Chau, J. L., Vierinen, J., Jacobi, C., & Wilhelm, S. (2018). Retrieving horizontally resolved wind fields using multi-static meteor radar observations. *Atmospheric Measurement Techniques*, 11, 4891–4907. https://doi.org/10.5194/amt-11-4891-2018
- Takahashi, H., Taylor, M. J., Pautet, P. D., Medeiros, A. F., Gobbi, D., Wrasse, C. M., et al. (2009). Simultaneous observation of ionospheric plasma bubbles and mesospheric gravity waves during the SpreadFEx Campaign. *Annals of Geophysics*, 27, 1477–1487. https://doi.org/10.5194/angeo-27-1477-2009
- Taylor, M. J., Eccles, J. V., LaBelle, J., & Sobral, J. H. A. (1997). High resolution OI (630 nm) image measurements of F-region depletion drifts during the Guara's Campaign. Geophysical Research Letters, 24, 1699–1702. https://doi.org/10.1029/97GL01207
- Thébault, E., Finlay, C. C., Beggan, C. D., Alken, P., Aubert, J., Barrois, O., et al. (2015). International geomagnetic reference field: The 12th generation. Earth, Planets and Space, 67, 79. https://doi.org/10.1186/s40623-015-0228-9
- Tsunoda, R. T. (2010). On equatorial spread F: Establishing a seeding hypothesis. Journal of Geophysical Research, 115. https://doi.org/10.1029/2010JA015564
- Valladares, C. E., Meriwether, J. W., Sheehan, R., & Biondi, M. A. (2002). Correlative study of neutral winds and scintillation drifts measured near the magnetic equator. *Journal of Geophysical Research*, 107(A7), 1112. https://doi.org/10.1029/2001JA000042
- Zalesak, S. T., Ossakow, S. L., & Chaturvedi, P. K. (1982). Nonlinear equatorial spread F: The effect of neutral winds and background Pedersen conductivity. *Journal of Geophysical Research*, 87(A1), 151–166. https://doi.org/10.1029/JA087iA01p00151

KARAN ET AL. 11 of 11